https://doi.org/10.5194/essd-2022-322
Preprint. Discussion started: 4 October 2022

Open Access Earth System Science Data Discussions

Spatial reconstruction of long-term (2003-2020) sea surface pCO_2 in the South China Sea using a machine learning based regression method aided by empirical orthogonal function analysis

Zhixuan Wang[1], Guizhi Wang[1,2], Xianghui Guo[1], Yan Bai[3], Yi Xu[1] and Minhan Dai[1,*]

[1]State Key Laboratory of Marine Environmental Science and College of Ocean and Earth Sciences, Xiamen University, Xiamen, 361102, China

[2]Fujian Provincial Key Laboratory for Coastal Ecology and Environmental Studies, Xiamen University, Xiamen, 361102, China

[3]State Key Laboratory of Satellite Ocean Environment Dynamics, Second Institute of Oceanography, State Oceanic Administration, Hangzhou, 310012, China

Correspondence to: Minhan Dai (mdai@xmu.edu.cn)

Abstract. The South China Sea (SCS), the largest marginal sea of the North Pacific Ocean, is one of the world's most studied model ocean margins in terms of its carbon cycle, where intensive field observations including sea-surface carbon dioxide partial pressure (pCO_2) have been conducted over the last two decades. However, the datasets of cruise-based sea surface pCO_2 are still temporally and spatially incomplete. Using a machine learning-based method facilitated by empirical orthogonal function (EOF) analysis capable of constraining the spatiality, this study provides a reconstructed dataset of the monthly sea surface pCO_2 in the SCS with a reasonably high spatial resolution (0.05º×0.05º) and temporal coverage between 2003 and 2020. We validate our reconstruction with three independent testing datasets where, TEST.1 includes 10% of our observed data, TEST.2 includes four independent underway datasets corresponding to four seasons, and TEST.3 includes a continuous observed dataset from 2003 – 2019 at the South East Asia Time-Series (SEATs) station located in the northern basin of the SCS. Our TEST.1validation demonstrated that the reconstructed pCO_2 field successfully simulated the spatial and temporal patterns of sea surface pCO_2. The root-mean-square error (RMSE) between our reconstructions and observed data in TEST.1 averaged to ~10 µatm, which is much smaller (by ~50%) than that between the remote sensing (RS) and observed data. TEST.2 verified the accuracy of our reconstruction model in data months lacking observations, showing a near-zero bias (RMSE: ~8 µatm). TEST.3 tested the accuracy of the reconstructed long-term trend, showing that at the SEATs Station, the difference between the reconstructed pCO_2 and observations ranged from -10 to 4 µatm (-2.5 to 1%). In addition to the typical machine learning performance metrics, we present a new method to assess the uncertainty that includes the bias from the reconstruction and its sensitivity to the features, and successfully quantifies the spatial distribution patterns of uncertainty. These validations and uncertainty analysis strongly suggest that our reconstruction is effectively captures the main features of both the spatial and temporal patterns of sea surface pCO_2 in the

https://doi.org/10.5194/essd-2022-322
Preprint. Discussion started: 4 October 2022

SCS. Using the reconstructed dataset, we show the long-term trends of sea surface pCO_2 in 5 sub-regions of the SCS with differing physico-biogeochemical characteristics. We show that mesoscale processes such as the Pearl River plume and China Coastal Currents significantly impact sea surface pCO_2 in the SCS during different seasons. While the SCS is overall a weak source of atmospheric CO_2, the northern SCS acts as a sink, showing a trend of increasing strength over the past two decades.

Key words: Sea surface pCO_2; reconstruction; machine learning; South China Sea

1 Introduction

The ocean possesses much of the global capacity for atmospheric carbon dioxide (CO_2) sequestration and annually mitigates 22–26% of the anthropogenic CO_2 emissions associated with fossil fuel burning and land use change during the period 1960–2019 (Friedlingstein et al., 2020). However, it remains largely unknown whether and by how much the ocean will continue to act as a sink for anthropogenic CO_2, i.e., the extent of its climate change mitigation capacity to understand climate-carbon coupled systems and develop zero-emission strategies and actions. Ocean margins, an essential part of the land-ocean continuum, contributed ~ 10-20% of the global ocean CO_2 sequestration with only 7% of the surface area and represent a particularly challenging regime (e.g., Chen and Borges, 2009; Dai et al. 2022; Laruelle et al., 2014). This is primarily attributed to the ocean margins' extremely complex and dynamic processes, often characterized by large spatial and temporal variability of air-sea CO_2 fluxes that lead to even larger uncertainty in their prediction than those occurring in the open ocean (Dai et al., 2013, 2022; Cao et al., 2020; Laruelle et al., 2014; Chen and Borges, 2009 and the references therein). Limited spatiotemporal coverage of observational data is an important source of these uncertainties.

In recent years, many studies use numerical models or data-based approaches to improve estimates of sea surface CO_2 distribution and the accuracy of the global carbon budget for periods and regions with poor coverage of observational data (Rödenbeck et al., 2015; Wanninkhof et al., 2013). Numerical ocean models of performance can successfully quantify the generally increasing trend in oceanic CO_2 and some critical processes of carbon cycling (e.g., net ecosystem production), but still suffer from regional and seasonal differences in their estimates of the ocean carbonate system (Luo et al., 2015; Mongwe et al., 2016; Tahata et al., 2015; Wanninkhof et al., 2013). Thus, data-based approaches have become a popular alternative to biogeochemical models (Jones et al., 2014; Lefèvre et al., 2005;Landschützer et al., 2014, 2017; Telszewski et al., 2009). The former typically use statistical interpolations and regression methods. Statistical interpolations improve the spatial coverage of observational data, but do not work for the period without observational data. Regression methods allow mapping of the relationship between the observed carbon dioxide partial pressure (pCO_2) data and other parameters that may drive changes in surface ocean pCO_2, and then extrapolation of this relationship to improve estimates of the spatiotemporal distribution of pCO_2. The development of machine learning methods and remote sensing-derived products (as proxy variables in regression methods) have aided the development of data-based methods (Rödenbeck et al., 2015; Bakker et al., 2016) which, with spatial-temporal standardization, can improve the

https://doi.org/10.5194/essd-2022-322
Preprint. Discussion started: 4 October 2022

model results of the oceanic carbonate system by numerical assimilation methods. However, because of the complex and dynamic nature of biogeochemical and physical processes in coastal areas, characterization of sea surface pCO_2 and subsequently the air-sea CO_2 fluxes both in time and space in marginal seas remains challenging.

The South China Sea (SCS) is the largest marginal sea of the North Pacific Ocean with a surface area of 3.5×10^6 km^2. Although extensive field observations have been conducted of sea surface pCO_2 in the SCS in the past two decades, their spatial and temporal coverage is still limited in different physical-biogeochemical domains of the SCS and at sub-seasonal time scales (e.g., Guo et al., 2015; Li et al., 2020; Zhai et al., 2005; Zhai et al., 2013). Therefore, there is a clear need to achieve surface water pCO_2 coverage in the SCS with a highest spatiotemporal resolution as possible with the aim to better estimate sea surface pCO_2 and thus air-sea CO_2 fluxes in the SCS and help develop improved initial conditions of numerical models. Moreover, a reasonably high spatiotemporal resolution of pCO_2 data can help identify the controlling factors of pCO_2 changes in the SCS, and reliably resolve the long-term changes.

Zhu et al. (2009) presented an empirical approach that estimated sea surface pCO_2 in the northern SCS in summer using satellite-derived data (sea surface temperature, SST; chlorophyll *a*, Chl *a*), and their validation results show that the reconstructed pCO_2 data was generally consistent with the underway observed data. However, it should be noted that the large uncertainty of estimates from their study was caused by the limited underway observed data from only two summer cruises (July 2000 data were used for algorithm tuning and those of July 2000 for validation). Jo et al. (2012) developed a neural networking-based algorithm by using SST and Chl *a* to estimate sea surface pCO_2 in the northern SCS. Sea surface pCO_2 data in this study were collected from May 2001, and, February, July 2004. The difference between the reconstructed pCO_2 data of Jo et al. (2012) and the observed data reflects a relatively large bias (the resultant RMSE (root-mean-square error) falls in the range 32.6 to 44.5 µatm, reported in Wang et al., 2021). Bai et al. (2015) used a 'mechanic semi-analytical algorithm' to estimate the satellite remote sensing-derived sea surface pCO_2 data in the East China Sea during 2000–2014, and then used this algorithm to estimate sea surface pCO_2 for the whole China Sea. These authors also pointed the limitation of their mechanistic semi-analytical algorithm (MeSAA) which did not fully account for some local processes and therefore causes errors (the RMSE is about 45 µatm in the SCS (reported in Wang et al., 2021). Bai et al. (unpublished) subsequently used a machine learning based non-linear regression to develop a retrieval algorithm for seawater pCO_2 in the China Sea, and the satellite-derived pCO_2 data from 2003-2018 were provided by the SatCO$_2$ platform (www.SatCO2.com) with a RMSE of 21.1 µatm in China Seas.

To take advantages of both the high spatiotemporal resolution of the remote sensing-derived pCO_2 data (RSdata) and the accuracy of the observational data, Wang et al. (2021) reconstructed the basin–scale sea surface pCO_2 in the SCS in summer by using the empirical orthogonal function (EOF) based on a multi-linear regression method and demonstrated the reliability of the reconstructions. However, when the spatial standard deviation of observed data is relatively large because of the influence of outliers, the reconstruction results may be biased (Wang et al., 2021). Therefore, many studies used the machine learning-based

https://doi.org/10.5194/essd-2022-322
Preprint. Discussion started: 4 October 2022

regression method to reduce the influence of outliers for open ocean areas, with a RMSE of <17 μatm in most cases (e.g., Zeng et al., 2017; Li et al., 2019).

Building upon the EOF method that significantly improved the reconstruction in terms of spatial pattern and accuracy (Wang et al., 2021), we developed a machine learning-based regression method facilitated by the EOF to fully resolve the long-term spatial distribution of sea surface pCO_2 at a resolution of 0.05º×0.05º in the SCS. In addition to the typical machine learning performance metrics, we present a novel uncertainty calculation method that incorporates the bias of both the reconstruction and the sensitivity of reconstructed models.

2 Study site and data sources

2.1 Study area

The SCS, located in the western Pacific, has a maximum water depth of ca. 4700 m (e.g., Gan et al., 2006, 2010). The rhombus deep-water basin with a southwest-northeast direction accounts for about half of the total area of the SCS (Fig. 1). The oceanography of the SCS is largely modulated by the Asian monsoon and the topography, thus exhibiting seasonally varying surface circulation, river inputs, and upwelling. Forced by the northeast winds in winter, the circulation of the upper layer shows a large cyclonic circulation structure (red solid line in Fig. 1), while in summer it exhibits an anticyclonic circulation structure forced by southwest winds (red dashed line in Fig. 1; Hu et al. 2010). In the northern SCS, the Pearl River discharges into the SCS with an annual freshwater input of 3.26×10^{11} m^3 (e.g., Dong et al., 2004; Dai et al., 2014). The area influenced by the Pearl River Plume may extend southeastward to a few hundred kilometers from the river estuary in summer because of the monsoon wind stress (Dai et al., 2014). The northern and western coastal regions of the SCS also feature summer coastal upwelling in summer, mainly including the Eastern Guangdong and Qiongdong upwelling systems in the northern SCS and the Vietnam upwelling systems in the western SCS (e.g., Cao et al., 2011; Chen et al., 2012; Gan et al., 2006; Gan et al., 2010; Li et al., 2020).

https://doi.org/10.5194/essd-2022-322
Preprint. Discussion started: 4 October 2022

Open Access Earth System Science Data Discussions

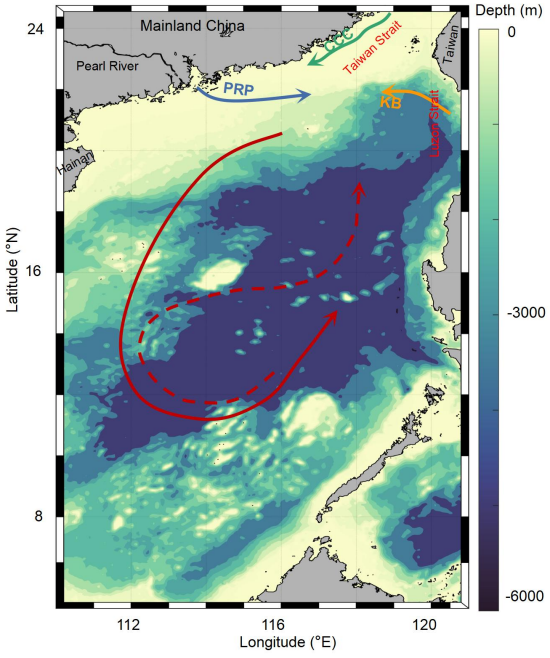

Figure 1. Topographic map of the South China Sea (SCS) showing a basin wide cyclonic gyre in winter (solid line) and an anticyclonic gyre over the southern half of the SCS in summer (dashed line). Also shown are the Kuroshio Branch (KB, orange line), the China Coastal Current (CCC, green line), and the Pearl River plume (PRP, blue line).

The SCS is a semi-enclosed sea basin with dynamic water exchange with the East China Sea via the Taiwan Strait and Western Pacific via the Luzon Strait (Fig. 1). In winter, driven by the winter monsoon, the China Coastal Current (CCC, yellow line in Fig. 1; Han et al., 2013; Yang et al., 2022) flows south along the Chinese mainland through the Taiwan Strait, and occupies the northern SCS with cold, fresh, nutrient-rich waters. The strong northeast winds in winter also slow down the western boundary ocean current, forcing the intrusion of Kuroshio water, which shows high surface salinity and high total alkalinity, into the SCS via the Luzon Strait (orange line in Fig. 1; Du et al., 2013; Park, 2013; Yang et al., 2022).

2.2 Observational pCO_2 data

Data collected from field surveys during the study period 2003-2020 are summarized in Table 1. Most observations were made in July, and fewer observations were made in March and December of each year. The rough sea state in the SCS in winter and early spring limited the survey during these seasons. Data collected from July 2000 to January 2018 were originally published by Li et al. (2020). The in situ pCO_2 were collected from R/Vs *Dongfanghong-2, Tan Kah Kee (TKK)*, etc. (shown in Table 1). The data collection methods used in this study have been introduced in Li et al. (2020). The spatial coverage and frequency of the observations are shown in Figure 2 and show that there are pronounced seasonal changes and that the data cover a large spatial area. For example, the spatial coverage of the observed data in spring and fall are relatively uniformly distributed, and the south end of the spatial coverage reaches 5 ºN in spring, whereas that during other seasons is concentrated in the northern and central

https://doi.org/10.5194/essd-2022-322
Preprint. Discussion started: 4 October 2022

regions of the SCS. In addition, only one observation was made in the basin area in winter, while the northern coastal area was more frequently surveyed, especially in summer.

Table 1. Summary of the seasonal observational data of sea surface pCO_2 in the South China Sea for the period 2003-2020 used in this study.

Season	Spring			Summer		
	March	April	May	June	July	August
Cruise time	2004.03	2005.04 2008.04 2009.04 2012.04 2020.04	2004.05 2011.05 2014.05 2020.05	2006.06 2016.06 2017.06 2019.06 2020.06	2004.07 2005.07 2007.07 2008.07 2009.07 2012.07 2015.07 2019.07	2007.08 2008.08 2019.08
Season	Fall			Winter		
	September	October	November	December	January	February
Cruise time	2004.09 2007.09 2008.09 2020.09	2003.10 2006.10	2006.11 2010.11	2006.12	2009.01 2010.01 2018.01	2004.02 2006.02

***Data were collected before February 2018 except those collected in July 2015 and June 2017 which are from Li et al. (2020).**

https://doi.org/10.5194/essd-2022-322
Preprint. Discussion started: 4 October 2022

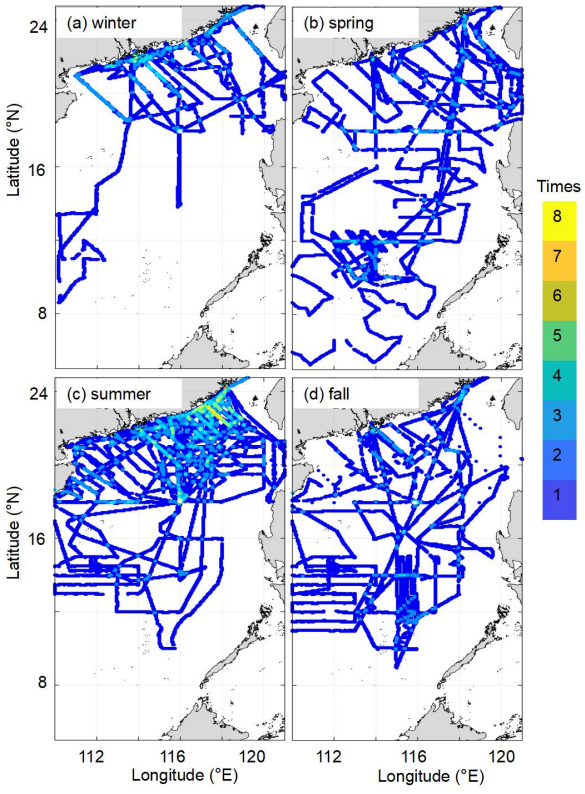

Figure 2. Cruise tracks of the observations conducted in the South China Sea in each season from 2000 to 2020: (a) winter, (b) spring, (c) summer, and (d) fall. The data were collected before February 2018 except those collected in July 2015, June 2017 which are from Li et al. (2020).

Figure 3 shows the spatial and temporal distributions of surface water pCO_2. Seasonally, the lowest pCO_2 occurs in January, and the highest concentrations occur in May and June. Spatially, the pCO_2 distribution in the basin is relatively homogeneous, but shows large variability in the northern region. In the northern coastal area in summer, the observed pCO_2 distribution is affected by the Pearl River plume (yielding low values) and coastal upwelling (yielding high values), which last into early fall. In winter and early spring, relatively low pCO_2 values were determined in the coastal area. In addition, the high pCO_2 values recorded on the western side of the Luzon Strait in December demonstrate the influence of winter upwelling during some of the surveys.

In addition to the above observational data, we selected four independent surveys corresponding to four seasons, and a continuous observation dataset during 2003–2019 at the Southeast Asia Time-Series (SEATs) station (Dai et al., 2022) as two important independent testing datasets.

https://doi.org/10.5194/essd-2022-322
Preprint. Discussion started: 4 October 2022

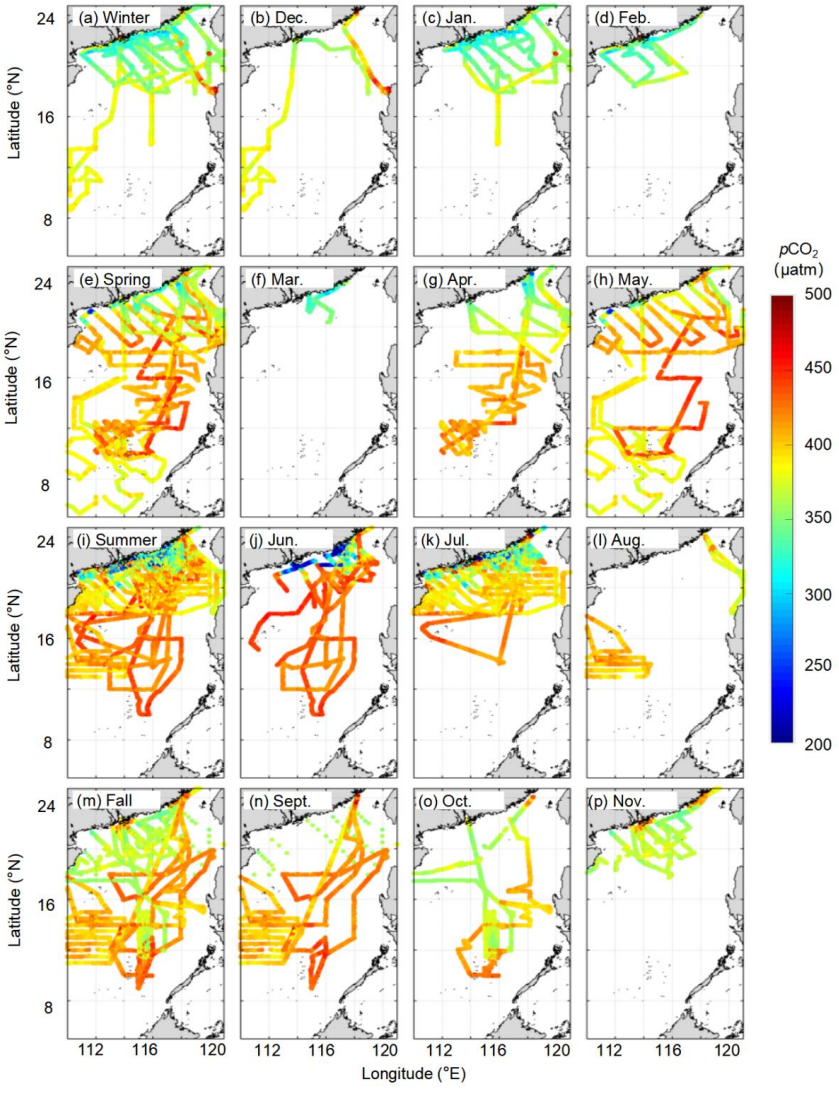

Figure 3. Seasonal and monthly sea surface pCO_2 fields in the South China Sea. The data sources can be found in Table 1.

2.3 Remote sensing-derived sea surface pCO_2 data

The gridded (0.05°×0.05°) remote sensing-derived pCO_2 data covered almost the entire SCS (5–25° N, 109–122° E), and show the major CO_2 variation at a large scale (Wang et al., 2021; Bai et al., unpublished). Further details of the remote sensing (RS) data can be found in the SatCO_2 platform (www.SatCO2.com).

A grid-to-grid comparison was undertaken (Fig. 4) and the RMSE of the RS data-derived pCO_2 values were compared with the observed pCO_2 data (Table 2). This comparison shows that the difference between the RS and the observed pCO_2 data ranges from

https://doi.org/10.5194/essd-2022-322
Preprint. Discussion started: 4 October 2022

35 to 120 μatm in the coastal area, and that the largest biases occur in summer. In terms of the RMSE (Table 2), the largest bias reaches 30.0 μatm in summer. Bai et al. (2015; unpublished) and Wang et al. (2021) pointed out that relatively large discrepancies may reflect the limitations of the current algorithm, which considers only biological processes and the turbidity induced by the Pearl River discharge (characterized by Chl *a* and the remote sensing reflectance at 555 nm (rrs555) and does not take into account the riverine dissolved inorganic carbon and the input of other substances that may affect pCO_2.

Because of the relatively large bias of RS data, their direct use may lead to overestimate pCO_2 values in the reconstructed field. In this study, the EOF method was used to compute the spatial patterns of the RS data to assess the accuracy and spatial distribution of the reconstruction data as a whole and remove the influence of the limited RS data.

Table 2. Biases between the seasonal remote sensing (RS)-derived pCO_2 data and observed pCO_2 data, and between the reconstructed and the observed underway pCO_2 data. (unit: μatm; the remote sensing-derived pCO_2 data during 2003-2019 are from www.SatCO2.com and the source of observed data can be found in Table1. The reconstructed pCO_2 data are from section 3; all data were gridded into 0.05°*0.05°; /: no data). MAE = mean absolute error; RMSE = root mean square error; R^2 = coefficient of determination; MAPE = mean absolute percentage error.

		RS	Training data	Testing data I	Testing data II	Testing data III
Spring	MAE	9.00	2.44	4.76	1.68	/
	RMSE	12.70	3.47	7.43	2.26	/
	R^2	/	0.98	0.92	/	/
	MAPE	/	0.01	0.01	/	/
Summer	MAE	16.75	2.48	8.46	5.73	/
	RMSE	29.956	3.54	14.69	15.18	/
	R^2	/	0.99	0.89	/	/
	MAPE	/	0.01	0.02	/	/
Fall	MAE	9.93	2.41	4.90	7.133	/
	RMSE	13.08	3.39	6.85	8.94	/
	R^2	/	0.98	0.92	/	/
	MAPE	/	0.01	0.01	/	/
Winter	MAE	9.25	2.18	5.61	11.41	/
	RMSE	14.26	3.14	8.82	12.63	/
	R^2	/	0.98	0.89	/	/

https://doi.org/10.5194/essd-2022-322
Preprint. Discussion started: 4 October 2022

	MAPE	/	0.01	0.01	/	/
Annual	MAE	11.95	2.41	6.30	5.27	6.19
	RMSE	20.66	3.43	10.79	11.18	8.26
	R^2	/	0.99	0.91	/	/
	MAPE	/	0.01	0.01	/	/

176

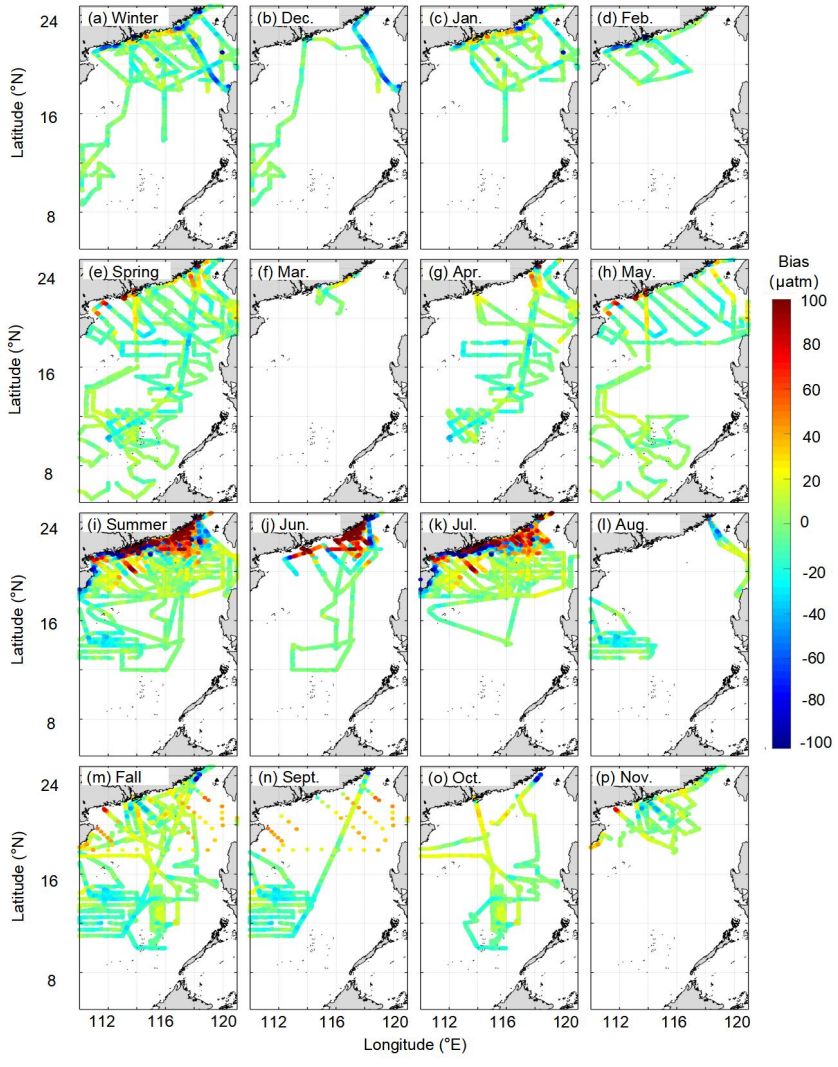

177

178 **Figure 4. Differences between the seasonal and monthly remote sensing-derived pCO_2 and the observed pCO_2 data (the**
179 **former during 2003-2019 is from www.SatCO2.com, and the source of observed data can be found in Table 1. Both**
180 **datasets are gridded into 0.05°×0.05°, and the bias is plotted grid by grid).**

https://doi.org/10.5194/essd-2022-322
Preprint. Discussion started: 4 October 2022

181

182 **2.4 Other data**

183 The RS SST data produced by MODIS (https://oceancolor.gsfc.nasa.gov/) are adopted here. The uncertainty of this dataset in the
184 SCS is ~0.27° (Qin et al., 2014). For the SSS data, Wang et al. (in preparation) found a relatively high differential between the
185 values found in different open source databases (i.e., multi-satellite fusion data from https://podaac.jpl.nasa.gov/; model data from
186 https://climatedataguide.ucar.edu/; multidimensional covariance model data from https://resources.marine.copernicus.eu/) and our
187 observed data. Wang et al. (in preparation) reconstructed a SSS database using machine learning methods based on the observation
188 dataset. The bias between the reconstructed SSS and observed data was near-zero (mean absolute error, MAE: ~0.25). Next, we
189 used Chl-*a* as an indicator of biological influence. Chl-*a* data from MODIS (https://oceancolor.gsfc.nasa.gov/) are adopted in the
190 present study, which have a bias of ~0.35 on log scale and ~115% in the SCS (Zhang et al., 2006). Atmospheric pCO_2 also
191 influences surface water pCO_2 through air–sea CO_2 exchange. We chose the atmosphere CO_2 mole fraction (xCO_2) data from the
192 monthly mean CO_2 concentrations measured at Mauna Loa Observatory, Hawaii (https://gml.noaa.gov/). The atmospheric pCO_2
193 values were calculated from xCO_2 using the method of Li et al. (2020).

194

195 **3 Methods**

196 The pCO_2 reconstruction procedure is shown in Figure 5. It includes: (1) data processing and (2) model training and testing. For
197 the former, we first gridded the observed and RS pCO_2 data into 0.05°×0.05° grid boxes with monthly temporal resolution.
198 Secondly, we used the pCO_2 filling method of Fay et al. (2021) to fill the missing pCO_2 measurements with the RS pCO_2 data. We
199 then used a feature engineering method to ignore any biases in the data itself or from the pCO_2 filling method. Thirdly, the gridded
200 observed pCO_2 data and their corresponding RS data were divided into a training set (90%) and a testing set (10%) to calculate the
201 pCO_2 reconstruction model. To ensure that the model had sufficient training samples in the coastal area, we divided the entire SCS
202 into two regions along the 200 m depth contour. The data from these two regions were divided into training and testing sets with
203 the same ratios listed above (9:1), which were then combined to obtain the final training and testing sets.

https://doi.org/10.5194/essd-2022-322
Preprint. Discussion started: 4 October 2022

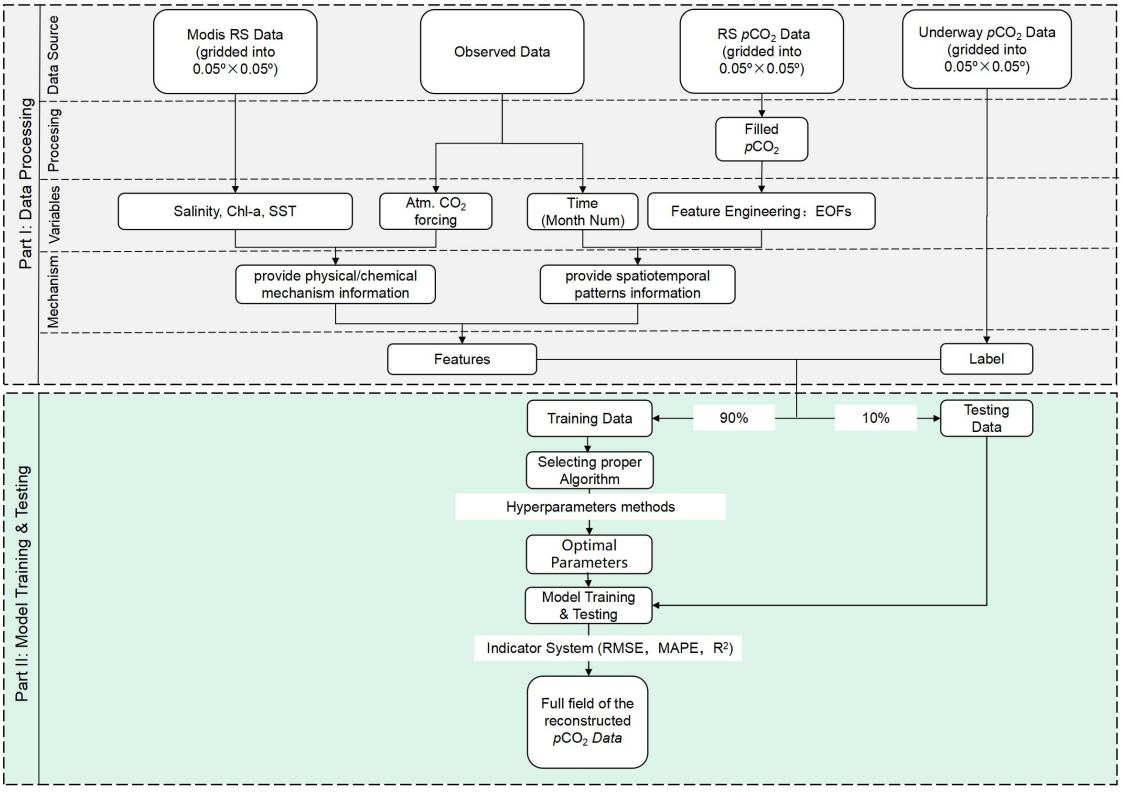

Figure 5. Procedure for the reconstruction of surface water pCO_2 using machine learning. RS data = remote sensing data, RMSE = root mean square error, MAPE= mean absolute percentage error, and R^2 = coefficient of determination, and MAE = average absolute error.

For model training and testing, we first chose a relatively reliable algorithm to undertake the pCO_2 reconstruction. After that, we determined the optimal range of the parameters using hyperparameter methods (code from https://github.com/optuna/) for the training set. The final optimal parameter values were then determined using the K-fold and cross validation method (code from https://github.com/suryanktiwari/Linear-Regression-and-K-fold-cross-validation) for the training set. These optimal parameters were applied to the chosen algorithm. Finally, the testing set was used to verify the accuracy of the pCO_2 reconstruction model produced by the training set, and some indicators of the model's accuracy were calculated. More detailed methods employed in the present study are described below.

3.1 Remote sensing data filling

As mentioned in the SatCO2 platform (www.SatCO2.com), the RS pCO_2 data are missing some values. Thus, we used the pCO_2 filling method suggested by Fay et al. (2021) to fill in the missing portions. First, a scaling factor for a filled month was calculated according to Eqation 1:

$$sf_{pCO2} = mean_{x,y}\left(\frac{pCO_2^{ens}}{pCO_2^{clim}}\right) \quad (1)$$

https://doi.org/10.5194/essd-2022-322
Preprint. Discussion started: 4 October 2022

where sf_{pCO2} is the scaling factor, pCO_2^{ens} is the monthly RS pCO_2 datum, and pCO_2^{clim} is the monthly climatology RS pCO_2 datum; x and y indicate that we took the area-weighted average over longitude (x) and latitude (y) to produce the monthly sf_{pCO2} value. Then, the filled portion of the data can be calculated from the pCO_2^{clim} data multiplied by the sf_{pCO2} value (see Fay et al. (2021) for details of this method).

Briefly, this filling method scales the climatological monthly pCO_2 field values to fill in the missing measurements. Therefore, although specific values may be biased, the interpolated measurements still retain the main spatial distribution pattern of the filled months.

3.2 Feature engineering and selection

As mentioned above, the pCO_2 filling method may bias some of the actual values. To avoid such biases, instead of directly using the RS pCO_2 data as features in our reconstructed model, we used the feengineered featured data (via the EOF method) to obtain the main spatiotemporal distribution patterns of the RS pCO_2 data as features in our reconstructed model. The EOF method can reflect the spatial commonality of variables shown in the time series. For each 12 months, the cumulative variance contribution of the first eight EOF values was consistently > 90%, indicating it that it could explain the main pCO_2 spatial characteristics during each month, and we therefore selected them as features.

The feature selection in our reconstructed model can be divided into two main categories. The first one is related to the underlying physicochemical mechanism controlling the pCO_2 distribution, and the other one can provide spatiotemporal information for pCO_2 reconstruction. For example, the SST dominating the seasonal variation in surface water pCO_2 in the northern SCS (Zhai et al., 2005; Chen et al., 2007; Li et al., 2020). Previous research (Landschützer et al., 2014; Laruelle et al., 2017; Denvil et al., 2019) shows that Chl-*a* plays a critical role in fitting the influence of biological activity to pCO_2, especially in the northern SCS (Landschützer et al., 2014; Laruelle et al., 2017; Denvil et al., 2019). Sutton et al. (2017) suggest that the increase in atmospheric pCO_2 controls the increase in seawater pCO_2. For the features that provide spatiotemporal information for pCO_2 reconstruction, whereas in the present study we selected the first eight EOF values of pCO_2 as the main spatial distribution feature and monthly information of the observed datasets as the temporal feature.

3.3 Algorithm selection

Ensemble learning provides one of the most powerful machine learning techniques (e.g., Zhan et al., 2022; Chen et a., 2020). It is the process of training multiple machine learning models and combining their output to improve the reliability and accuracy of predictions (e.g., Zhan et al., 2022; Chen et a., 2020). Different models are used as the basis to develop an optimal predictive model. There are two main ways to employ ensemble learning: bagging (to decrease the model's variance) or boosting (to decrease the model's bias). The random forest algorithm (code from https://scikit-learn.org/stable/) is an extension of the bagging method as it utilizes both bagging and feature randomness to create an uncorrelated forest of decision trees. The Light Gradient Boosting Machine (LightGBM; code from https://github.com/microsoft/LightGBM/) is a gradient boosting framework that uses

https://doi.org/10.5194/essd-2022-322
Preprint. Discussion started: 4 October 2022

tree-based learning algorithms. LightGBM can be used for regression, classification, and other machine learning tasks; it exhibits rapid and high-performance as a machine learning algorithm. CATBOOST (code from https://github.com/catboost/) is a gradient boosting algorithm, which improves prediction accuracy by adjusting weights according to the data distribution and by incorporating prior knowledge about the dataset. This can help to reduce overfitting and improve generalization performance.

From the above options, we chose three ensemble learning algorithms as the machine learning-based regression portion, and multi-linear regression methods (Wang et al., 2021) as the linear regression portion, and we then used the K-fold and cross validation methods to verify the applicability of the different regression algorithms in the pCO_2 reconstruction of summer training data in the SCS, since the greatest temporal sampling coverage occurs in summer (Table 1; Fig. 2). Results show that the CATBOOST algorithm yields the best degree of accuracy, with an RMSE of 16 μatm; for comparison, the RMSE of LightGBM was 27 μatm, that of Random Forest was 26 μatm, and nearly 20 μatm was found for the linear regression algorithm employed by Wang et al. (2021). Thus, CATBOOST appears to provide a relatively reliable algorithm for pCO_2 reconstruction.

3.4 Evaluation metrics

It is necessary to evaluate the accuracy of any model based on certain error metrics before applying it to specific scenarios. Common model evaluation metrics include RMSE, MAPE , R^2 (coefficient of determination), and MAE.

The mean squared error (MSE) stands for the standard deviation of the residuals (prediction error), where the residuals represent the distance between the fitted line and the data point.i.e., it stands for the degree of concentration of the reconstructed data around the regression line. In regression analysis, RMSE is commonly used to verify experimental results. To assess bias, the RMSE needs to combine the magnitude of the model data and is calculated as:

$$\mathrm{RMSE} = \sqrt{\frac{1}{n}\sum_{i=1}^{n}(y_i - y_{ri})^2} \quad . \qquad (2)$$

where y stands for the observational data, y_r represents the reconstructed data, and n is the number of data.

The mean absolute percentage error (MAPE) is a statistical measure used to define the accuracy of a machine learning algorithm on a particular dataset. It is commonly used because, compared to other metrics, it uses a percentage to measure the magnitude of the bias and is easy to understand and interpret; the lower the value of MAPE, the better a model is at forecasting. MAPE is calculated as follows:

$$\mathrm{MAPE} = \frac{1}{n}\sum_{i=1}^{n}\frac{|y_i - y_{ri}|}{|y_i|} \qquad (3)$$

The regression error metric, the coefficient of determination R^2, can describe the performance of a model by evaluating the accuracy and efficiency of modeled results, i.e., it indicates the magnitude of the dependent variable calculated by the regression model that can be explained by the independent variable, and is calculated as:

https://doi.org/10.5194/essd-2022-322
Preprint. Discussion started: 4 October 2022

$$R^2 = 1 - \frac{\sum_{i=1}^{n}(y_i - \overline{y_i})^2}{\sum_{i=1}^{n}(y_i - y_{ri})^2} \quad (4)$$

MAE is the average absolute difference between the field observations (true values) and model output (predicted values). The sign of these differences is ignored so that cancellations between positive and negative values do not occur. It is calculated as:

$$MAE = \frac{1}{n}\sum_{i}^{n} | y_i - y_{ri} | \quad (5)$$

4 Results and discussion

4.1 Results

The reconstructed pCO_2 fields show relatively low values in the northern coastal study region but generally shows high values in the mid and southern basins (Fig. 6). The continuity changes of the spatiotemporal distribution can be found in the reconstruction results (Fig. 6). The reconstructed pCO_2 fields show a trend of slow but sustained increase from 2003 to 2020. Spatial patterns of pCO_2 change between 2003 and 2020, such that the coastal portion of the northern SCS shows relatively complex variability because of multiple controlling factors, such as coastal upwelling, river plumes, biological activity, etc. However, pCO_2 values in the mid and southern basin are relatively homogeneous, because they are mainly controlled by atmospheric CO_2 forcing and SST. Temporal changes in pCO_2 between 2003 and 2020, are relatively large (~44 μatm) in summer and relatively small (~33 μatm) in winter.

https://doi.org/10.5194/essd-2022-322
Preprint. Discussion started: 4 October 2022

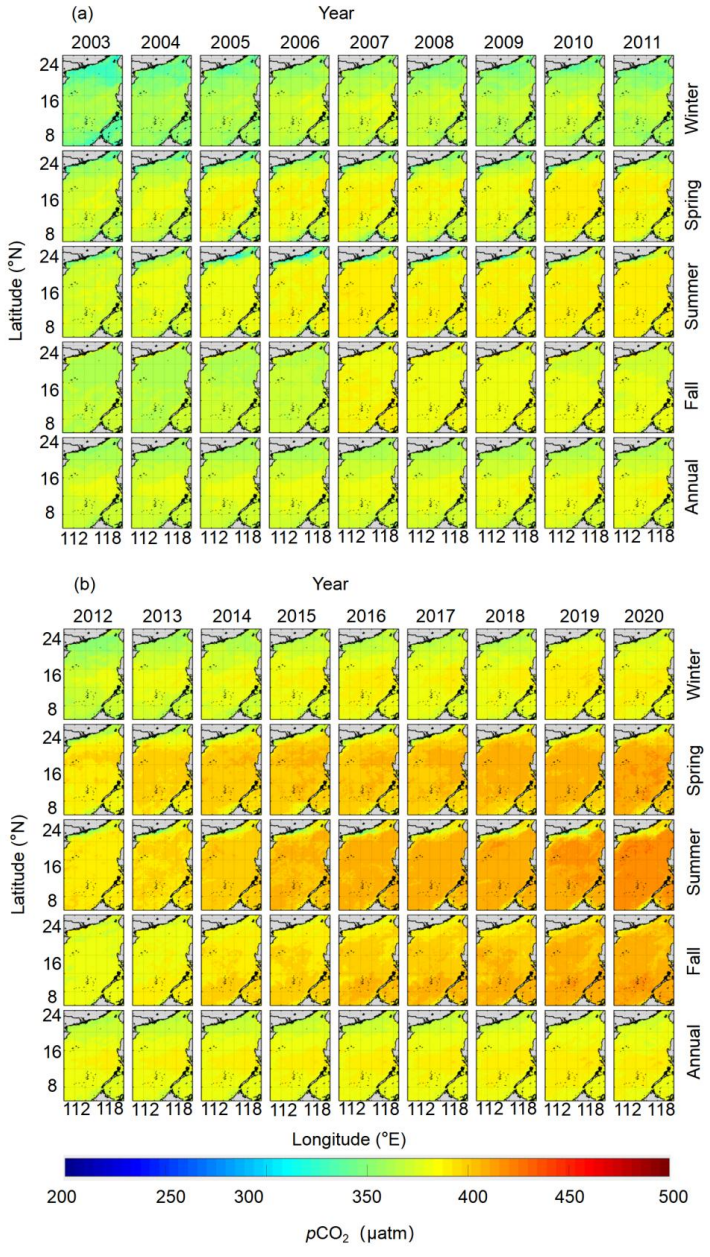

Figure 6. Reconstructed seasonal and annual pCO_2 fields in the South China Sea during the period 2003 to 2020 (a, 2003-2011; b, 2012-2020).

4.2 Model validation

Figure 7 compares the reconstructed and field-observed data. For the training dataset, the reconstructed pCO_2 fields of the four seasons fit the field-observed data well (Fig. 7), with an average RMSE of 3.43 μatm and an average MAE of ~2 μatm (Table 2). For the testing sets, although there are some outliers, most of the reconstructed pCO_2 data are consistent with field-observed data,

https://doi.org/10.5194/essd-2022-322
Preprint. Discussion started: 4 October 2022

302 with RMSE averaging 10.79 μatm and MAE averaging 6.30 μatm. The R^2 of the testing set is ca. 0.91. In terms of MAPE, the
303 accuracies of the four seasonal models are all around 99% (Table 2), with the highest value for spring data and the lowest value
304 for summer data. The greatest bias in the summer may be the influence of relatively complex regional processes, such as river
305 plumes and upwelling. The four evaluation metrics indicate that our reconstructed pCO_2 field is highly accurate in simulating both
306 the training and testing sets.

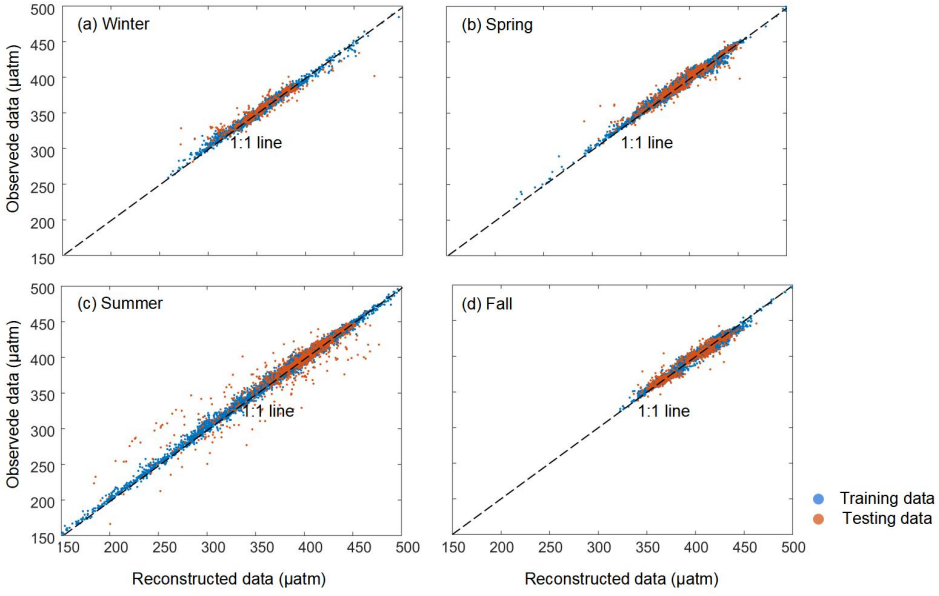

307

308 **Figure 7. Comparison between the reconstructed and the observed pCO_2 values.**

309 The distribution pattern of the biases between the reconstructed fields and the field observations in both training and testing
310 datasets can be found in Figure 8. In terms of the temporal distribution pattern, the biases are concentrated mainly in summer. For
311 the spatial distribution pattern, the biases in the northern coastal area are much greater than those in the basin. However, 95% of
312 the biases are < ±10 μatm. Therefore, our reconstruction data exhibit relatively high accuracy.

313

https://doi.org/10.5194/essd-2022-322
Preprint. Discussion started: 4 October 2022

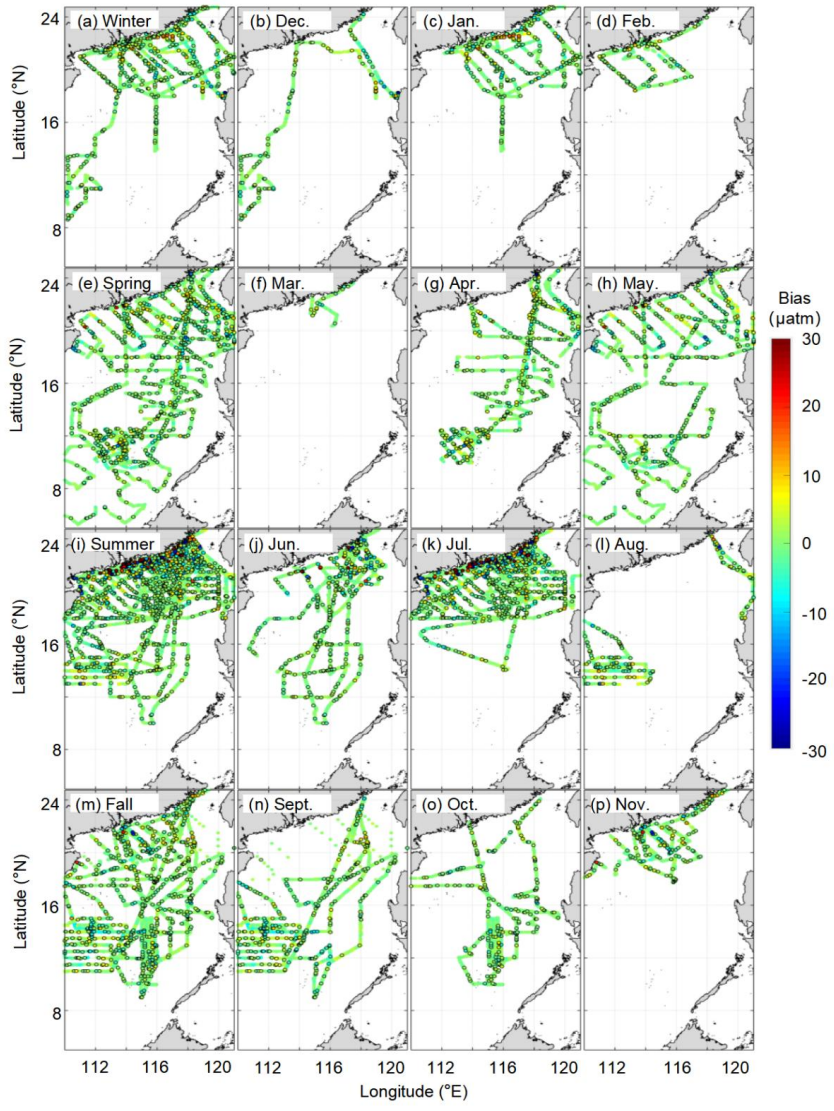

Figure 8. Differences between the seasonal and monthly reconstructed pCO_2 and the observed pCO_2 data. The open circles represent the difference between the training set and observational data, and the solid black circles represent difference between the test set and observational data.

.

Figure 9 shows the bias between our reconstructed fields and the four independent field observation datasets corresponding to the four seasons. This validation can verify the accuracy of the reconstruction model in data months with no observations, namely the applicability of the reconstruction model extrapolation. This comparison shows that the reconstruction model is relatively accurate in the basin, with a near-zero bias (MAE: ~8 μatm, Fig. 9 a). The greatest bias occurs in the Pearl River plume area in

https://doi.org/10.5194/essd-2022-322
Preprint. Discussion started: 4 October 2022

summer. The reconstruction model also has high accuracy in tpCO_2 spatial variation trends, except in the Pearl River plume area in summer (22–20 ºN), as shown in Fig. 9 b–e). The effect of the Pearl River plume on the pCO_2 spatial distribution in our reconstruction model is smaller than that shown by the field-observed data. This is because at around the survey time (August 24–28, 2019), a large amount of precipitation (~30mm/day; https://psl.noaa.gov/data/gridded/data.ncep.reanalysis2.surface.html) occurred around the Pearl River estuary region (24–20 ºN), which led to intensification of the Pearl River plume, such that the plume with relative low CO_2 values eventually decreased the observed values. However, the monthly average runoff of the Pearl River during that month (August, 2019; http://www.pearlwater.gov.cn/; Pearl River Plume Index in Wang et al., in preparation) is low, indicating that our reconstruction model is still highly reliable from the a monthly average perspective. Thus, the inconsistency between the reconstructed (monthly average) and field-observed datasets is mainly due to the differences in the time scales of the remote sensing and the field-observed data. The reconstructed data in this study were determined on a monthly scale, while the temporal resolution of the field-observed data was on the order of hours. It is clear that relatively pronounced short-term changes in pCO_2, such as the diurnal variation caused by short-term heavy precipitation, cannot be reflected in the reconstructed data.

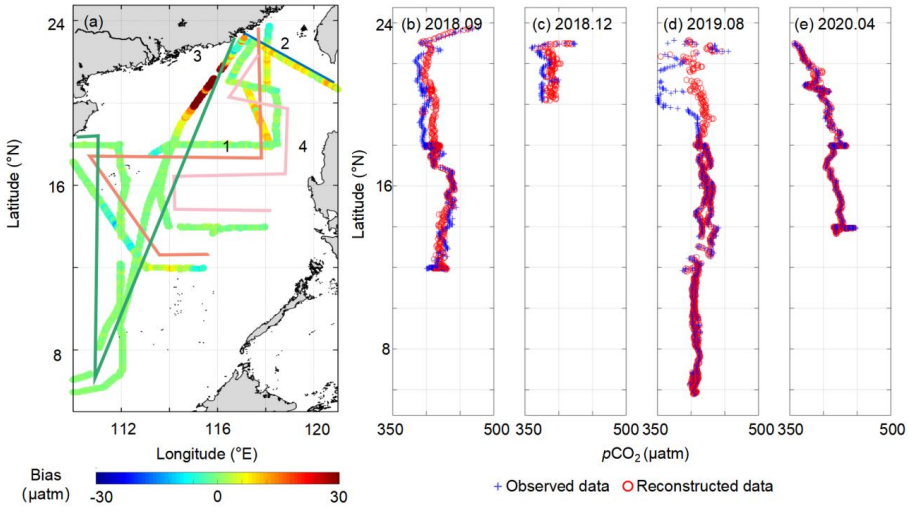

Figure 9. Difference between the reconstructed pCO_2 data and four independently observed datasets during the four seasons. In (a), the numbers 1–4 represent September (2018.9, b), December 2018 (2018.12, c), August 2019 (2019.8, d), and April 2020 (2020.4, e), respectively.

Dai et al. (2022) produced a time-series of observed data from 2003 to 2019 at the SEATs station, which we used here to validate the accuracy of the long-term trends of our model data (results shown in Fig. 10). The long-term trend of reconstructed pCO_2 data at the SEATs station are largely consistent with the observations, with differences mainly found before 2005. Thus, the long-term trend of our reconstructed model is also highly reliable.

https://doi.org/10.5194/essd-2022-322
Preprint. Discussion started: 4 October 2022

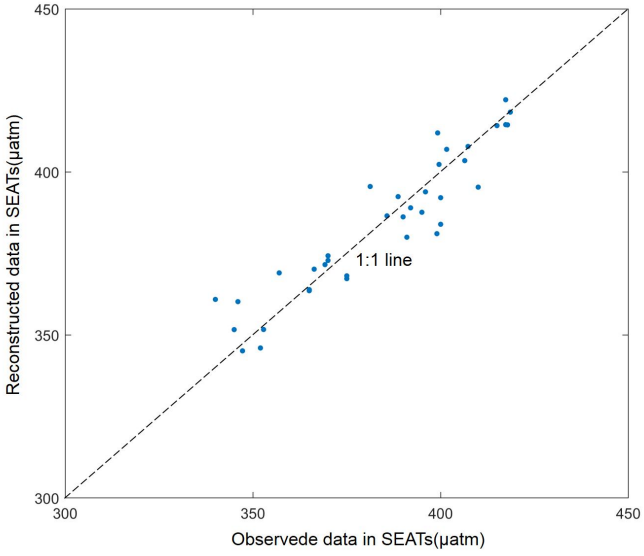

Figure 10. Comparison of the reconstructed pCO_2 with the observations at the Southeast Asia Time Series (SEATs) station (116◦ E, 18◦ N). The observed data are from Dai et al. (2022), which were calculated from dissolved inorganic carbon and total alkalinity.

4.3 Uncertainties

In previous studies, RMSE and MAE were mostly used to represent the uncertainties in the reconstructed data. As shown in Table 2, our reconstruction data have a high degree of accuracy, with an RMSE of ~10 μatm and MAE of ~6 μatm. However, this expression of uncertainty ignores the sensitivity of the reconstructed model to the features; i.e., the bias that the features themselves pass to the reconstructed model are ignored. Moreover, it is clearly unreasonable to use a single RMSE or MAE value to represent the entire region because the spatial bias patterns clearly differ between coastal and basin areas (Figs. 8 and 9).

Thus, we here present a novel method of uncertainty calculation as shown below:

$$Uncertainty = MAX\left(\frac{\sum_{i=1,j=1}^{n}\frac{|OR\_Monthly\_Data(i,j)-Obs\_Monthly\_Data(i,j)|}{Obs\_Monthly\_Data(i,j)}}{num(i)+num(j)}\right) * 100\% * pCO2\_recon \quad \text{(part 1)}$$

$$+ \quad \left(\frac{\partial pCO2}{\partial Feature}\right) dFeature \quad \text{(part 2).} \qquad (6)$$

Equation (7) includes two parts; the first is the conservative bias between the reconstructed pCO_2 fields and the observations (part 1), and the second is the sensitivity of the reconstructed model to the features (part 2). For part 1, $OR\_Monthly\_Data(i,j)$ stands for the monthly reconstructed data at longitude(i) and latitude(j), and $Obs\_Monthly\_Data(i,j)$ stands for the monthly observed data at longitude (i) and latitude (j). Therefore, the conservative bias is the maximum value of the monthly error ratio between the observed data and the reconstructed data. For part 2, where $dFeature$ stands for the bias of the features, we conducted a sensitivity analysis using a chain rule to evaluate the influence of these bias in the features on pCO_2. The bias of RS pCO_2 is ~21

https://doi.org/10.5194/essd-2022-322
Preprint. Discussion started: 4 October 2022

364 µatm (Table 2), the bias of SST is ~ 0.27° (Qin et al., 2014), that of SSS is ~0.33 (Wang et al., in prep.), and that of Chl-*a* is
365 ~115% (Zhang et al., 2006). We then estimated pCO_2 changes due to these features' variability by constraining these features
366 based on our model, and computing $\frac{\partial pCO2}{\partial Feature}$. For example, for the $\frac{\partial pCO2}{\partial SST}$ part, we only changed the value of SST, and kept the
367 value of the other features constant, to calculate the effect of each additional unit of SST on the results of the pCO2 simulation.
368 These two parts were then added together to obtain the final uncertainty, and results are displayed in Figure 11. The uncertainties
369 are greater in the coastal area (~13 µatm), than in the basin (~10 µatm). The spatial pattern of the uncertainty is consistent with
370 that shown in Section 4.2.

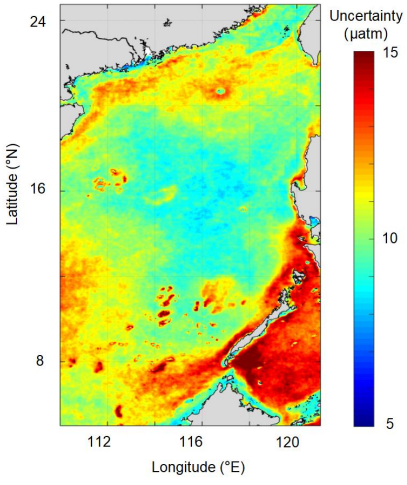

371

372 **Figure 11. Uncertainties of the reconstructed pCO_2 fields.**

373

374 **4.4 Spatial and temporal pCO_2 features**

375 The climatological monthly reconstructed pCO_2 fields are shown in Figure 12. The highest values of the reconstructed pCO_2 fields
376 occur in May and June, and the lowest value occurs in January. In winter, pCO_2 first decreases in December and then increases in
377 January; the pCO_2 value is ca. 325 µatm in the northern coastal area, and ca. 350 µatm in the basin. In spring, pCO_2 gradually
378 increases from the basin to the northern coastal area, and the basin high-value center gradually expands outward starting in April.
379 In summer, pCO_2 gradually declines starting in June. In fall, pCO_2 increases from north to south, and the southern region shows
380 consistently high values.

https://doi.org/10.5194/essd-2022-322
Preprint. Discussion started: 4 October 2022

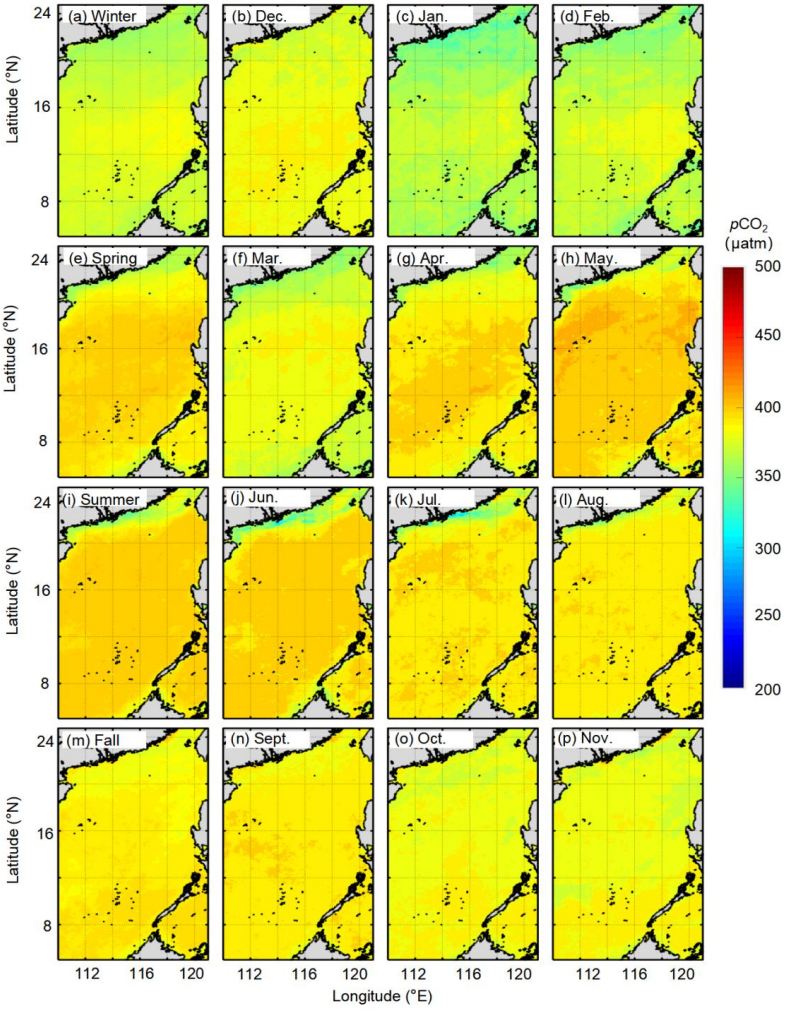

Figure 12. Long-term (2003–2020) seasonal and monthly average pCO_2 field (unit: µatm).

To better show specific regions in the northern coastal area, we zoomed in on the reconstructed pCO_2 fields at locations north of 18°N (Fig. 13). The reconstructed pCO_2 fields successfully reflect the influence of the meso-small scale processes on pCO_2 in this northern coastal area of the SCS. For example, in winter, the relatively low pCO_2 values, which last into early spring, are mainly controlled by the low SST, and the high pCO_2 around Luzon Strait affected by winter upwelling. In summer, the reconstructed pCO_2 field shows that the influence of the Pearl River plume on pCO_2 is the strongest in July and lasts until September; it also effectively shows the influence of coastal upwelling in the northeastern shelf (~23°N, 117°E). Thus, our reconstructed pCO_2 fields clearly reflect the spatial pattern of the field observed pCO_2 (Fig. 3), which are generally consistent with previously reported patterns (Li et al., 2020; Zhai et al., 2013; Gan et al., 2010).

https://doi.org/10.5194/essd-2022-322
Preprint. Discussion started: 4 October 2022

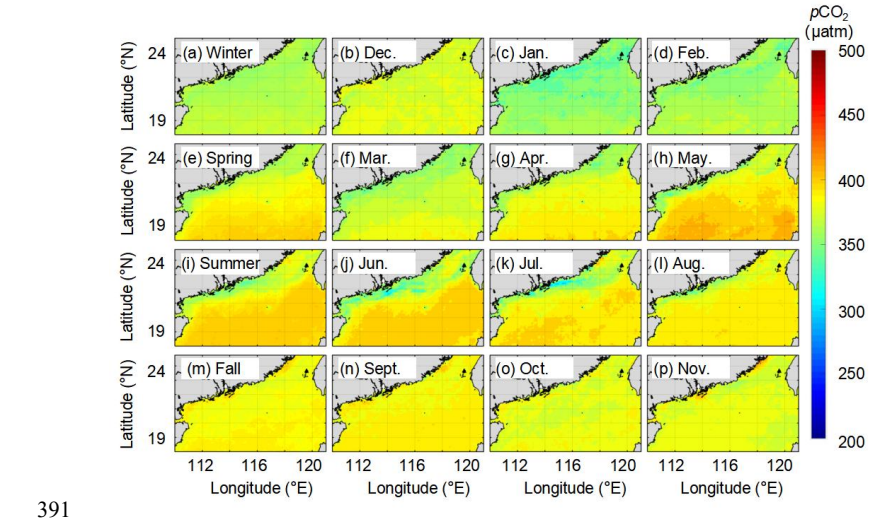

391

392 **Figure 13. Long-term (2003–2020) seasonal and monthly averaged pCO_2 field in the region north of 18°N (unit: µatm).**

393

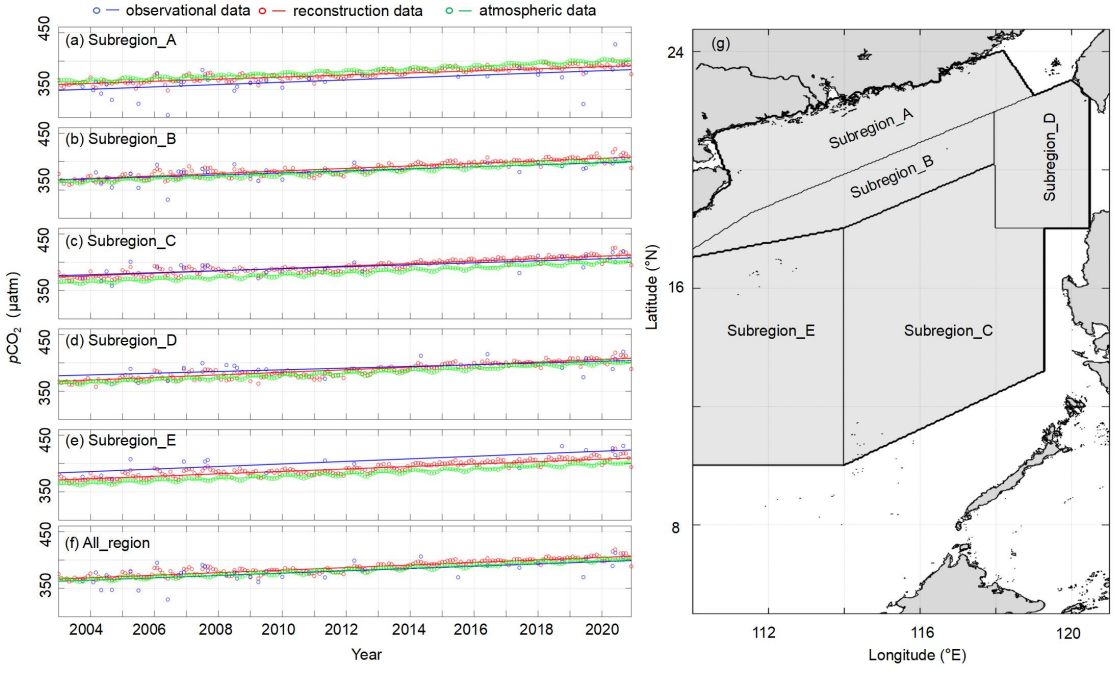

394

395 **Figure 14. Time series of Spatially averaged monthly pCO_2 data in five subregions (a-e) and the entire South China Sea (f)**
396 **under study. The subregions are shown in (g). The lines indicate the deseasonalized long-term trend of the spatially**
397 **averaged monthly pCO_2 data for each sub-region with the slopes shown in Table 3. The deseasonalized method can be**
398 **found in Landschützer et al., 2016.**

https://doi.org/10.5194/essd-2022-322
Preprint. Discussion started: 4 October 2022

Table. 3 Deseasonalized long-term trend of the spatially averaged monthly pCO_2 data for each sub-region of the South China Sea. (unit: µatm yr-1).

	All_region	A_region	B_region	C_region	D_region	E_region
Reconstructed	2.12±0.17	1.82±0.14	2.23±0.12	2.17±0.12	2.20±0.13	2.16±0.13
Observation	2.10±0.79	1.80±0.86	1.73±0.84	1.81±0.85	1.41±1.16	2.13±1.10

We divided SCS into five sub-regions according to Li et al. (2020). In Fig.14, region A stands for the northern coastal area of the SCS, region B stands for the slope area of the northern SCS, region C stands for the SCS basin, region D stands for the region West of the Luzon Strait, and region E stands for the slope and basin area of the western SCS. "All_region" indicates the whole region containing the five sub-regions described above. We then calculated the deseasonalized long-term trend of spatially averaged monthly data for each sub-region, and the results are shown in Figure 14 and Table.3. This deseasonalized trend is consistent with that of observational data, and its uncertaintyis on the 95% confidence interval much lower than that shown by the observational data. We can thus also infer that the long-term trend of our reconstructed data shows high reliability in all sub-regions, and that our data can serve as an important basis for predicting future changes of pCO_2 in the SCS.

In Fig.14 a-e, we found that the sea surface pCO_2 of the entire SCS is slightly higher than the atmospheric pCO_2, indicating that the SCS is a weak source of atmospheric CO_2. This conclusion is consistent with previous studies (e.g., Li et al., 2020). Moreover, compared to the rate of atmospheric CO_2 increase (~2.2 µatm yr-1), for region A, the pCO_2 trend is much slower than that of atmospheric pCO2, and the spatially averaged monthly mean pCO_2 is lower than the atmospheric pCO2. Thus, carbon accumulation in this region is expected to increase in future. For regions C and E, the spatially averaged monthly mean pCO_2 is higher than the atmospheric pCO2; thus, these two regions will still provide a weak source of atmospheric CO_2 in future. Finally, whether regions B and D act as a source or sink of atmospheric CO_2 is influenced by seasonal changes and physical processes.

5 Data availability

The data (the reconstructed CO_2 data, the Observational CO_2 data, and the remote sensing derived CO_2 data) for this paper are available under the link https://github.com/Elricriven/co2data (Wang et al., 2022).

6 Conclusions

Based on the machine learning method, we reconstructed the sea surface pCO_2 fields in the SCS with high spatial resolution (0.05*0.05°) over the last two decades (2003-2020) by calculating the statistical relationship between the underway observational pCO_2 data and remote sensing data. The machine learning method used in this study was facilitated by the EOF method, because

https://doi.org/10.5194/essd-2022-322
Preprint. Discussion started: 4 October 2022

the latter can provide spatial constraints for the data reconstruction. In addition to the typical machine learning performance metrics, we present a novel uncertainty calculation method that incorporates the bias of both the reconstruction and the sensitivity of reconstructed models to its features. This method effectively shows the spatiotemporal patterns of bias, and makes up for the spatial representation of the typical performance metrics.

We validate our reconstruction with three independent testing datasets, and the results show that the bias between our reconstruction and observational pCO_2 data in the SCS is relatively small (about 10 μatm). Our reconstruction successfully shows the main features of the spatial and temporal patterns of pCO_2 in the SCS, indicating that we can use these reconstructed data to further analyse the effect of meso-microscale processes (e.g., the Pearl River plume, and CCC) on sea surface pCO_2 in the SCS.

We divided the SCS into five sub-regions and separately calculated the deseasonalized long term trend of pCO_2 in each subregion, and compared them with the long-term trend of atmospheric pCO_2. Our results show that the reconstructed data are consistent with those of observational data. Moreover, the strength of the CO_2 sink in the northern SCS shows an increasing trend, whereas pCO_2 trends in other subregions are essentially the same as that of atmospheric pCO_2.

This high spatiotemporal resolution of sea surface pCO_2 data is helpful to clarify the controlling factors of pCO_2 change in the SCS and may be useful to predict changes of CO_2 source or sink patterns in this system.

Author contribution

Minhan Dai conceptualized and directed the field program of in situ observations. Xianghui Guo and Yi Xu participated in the in situ data collection. Yan Bai provided the remote sensing-derived pCO_2 data. Minhan Dai, Guizhi Wang and Zhixuan Wang developed the reconstruction method, wrote the codes, analyzed the data, and plotted the figures. Zhixuan Wang wrote the manuscript. Minhan Dai and Xianghui Guo contributed to the writing, editing and revision of the original manuscript.

Competing interests

The authors declare that they have no conflict of interest.

Acknowledgements

We thank the support of the National Natural Science Foundation of China (grant No. 42188102, 42141001, and 41890800), and the National Basic Research Program of China (973 Program, grant No.2015CB954000).

References

Bai, Y., Cai, W., He, X., Zhai, W., Pan, D., Dai, M., and Yu, P.: A mechanistic semi-analytical method for remotely sensing sea surface pCO_2 in river-dominated coastal oceans: A case study from the East China Sea, J. Geophys. Res.: Oceans, 120,

https://doi.org/10.5194/essd-2022-322
Preprint. Discussion started: 4 October 2022

2331-2349, 2015.

Bakker, D., Pfeil, B., Landa, C., Metzl, N., and Xu, S.: A multi-decade record of high-quality fCO_2 data in version 3 of the Surface Ocean CO2 Atlas (SOCAT), Earth Syst. Sci. Data, 8, 383-413, 2016.

Borges, A. V., Delille, B., and Frankignoulle, M.: Budgeting sinks and sources of CO_2 in the coastal ocean: Diversity of ecosystems counts, Geophys. Res. Lett., 32, L14601, 2005.

Cao, Z. and Dai, M.: Shallow-depth $CaCO_3$ dissolution: Evidence from excess calcium in the South China Sea and its export to the Pacific Ocean, Global Biogeochem. Cy., 25, GB2019, 2011.

Cao, Z., Dai, M., Zheng, N., Wang, D., Li, Q., Zhai, W., Meng, F., and Gan, J.: Dynamics of the carbonate system in a large continental shelf system under the influence of both a river plume and coastal upwelling, J. Geophys. Res.: Biogeo., 116, G02010, 2011.

Cao, Z., Yang, W., Zhao, Y., Guo, X., Yin, Z., Du, C., Zhao, H., and Dai, M.: Diagnosis of CO_2 dynamics and fluxes in global coastal oceans, Natl. Sci. Rev., 7, 786-797, 2020.

Chen, C. and Borges, A. V.: Reconciling opposing views on carbon cycling in the coastal ocean: Continental shelves as sinks and near-shore ecosystems as sources of atmospheric CO_2, Deep-Sea Res. I, 56, 578-590, 2009.

Chen, C., Lai, Z., Beardsley, R. C., Xu, Q., Lin, H., and Viet, N. T.: Current separation and upwelling over the southeast shelf of Vietnam in the South China Sea, J. Geophys. Res.: Oceans, 117, C03033, 2012.

Chen, F., Cai, W. J., Benitez-Nelson, C., and Wang, Y.: Sea surface pCO_2？-SST relationships across a cold-core cyclonic eddy: Implications for understanding regional variability and air-sea gas exchange, Geophys. Res. Lett., 341, 265-278, 2007.

Cheng, C., Xu, P. F., Cheng, H., Ding, Y., Zheng, J., Ge, T., and Xu, J.: Ensemble learning approach based on stacking for unmanned surface vehicle's dynamics. Ocean Eng., 207, 107388, 2020.

Dai, M. H., Cao, Z., Guo, X., Zhai, W., Liu, Z., Yin, Q., Xu, Y., Gan, J., Hu, J., and Du, C.: Why are some marginal seas sources of atmospheric CO_2?, Geophys. Res. Lett., 40, 2154-2158, 2013.

Dai, M., Gan, J., Han, A., Kung, H., and Yin, Z.: "Physical Dynamics and Biogeochemistry of the Pearl River Plume"" in Biogeochemical Dynamics at Large River-Coastal Interfaces. Eds. T. Bianchi, M. Allison and W. J. Cai (Cambridge University Press, Cambridge), 321-352, 2014.

Dai, M., J. Su, Zhao,Y., Hofmann, E. E., Cao, Z., Cai, W., Gan, J., Lacroix, F., Laruelle, G., Meng, F., Müller, J., Regnier, P., Wang, G., and Wang, Z.: Carbon fluxes in the coastal ocean: Synthesis, boundary processes and future trends, Annu. Rev. Earth Pl. Sc., 50, 593-626, 2022.

Du, C., Liu, Z., Dai, M., Kao, S. J., and Li, Y.: Impact of the Kuroshio intrusion on the nutrient inventory in the upper northern South China Sea: insights from an isopycnal mixing model, Biogeosciences, 10, 6419-6432, 2013.

Dong, L., Su, J. Wong, L. Cao, Z. and Chen, J.: Seasonal variation and dynamics of the Pearl River plume, Cont. Shelf

https://doi.org/10.5194/essd-2022-322
Preprint. Discussion started: 4 October 2022

Res., 24, 1761-1777, 2004.

Fassbender, A. J., Rodgers, K. B., Palevsky, H. I., and Sabine, C. L.: Seasonal Asymmetry in the Evolution of Surface Ocean pCO_2 and pH Thermodynamic Drivers and the Influence on Sea-Air CO_2 Flux, Global Biogeochem. Cy., 32, 1476-1497, 2018.

Fay, A., Gregor, L., Landschützer, P., McKinley, G., Gruber, N., Gehlen, M., Iida, Y., Laruelle, G., Rödenbeck, C., Roobaert, A., and Zeng, J.: SeaFlux: harmonization of air-sea CO2 fluxes from surface pCO_2 data products using a standardized approach, Earth Syst. Sci. Data, 13, 4693-4710, 2021

Friedlingstein, P., Jones, M. W., O'Sullivan, M., Andrew, R. M., Hauck, J., Peters, G. P., Peters, W., Pongratz, J., Sitch, S., Le Quéré, C., Bakker, D. C. E., Canadell, J. G., Ciais, P., Jackson, R. B., Anthoni, P., Barbero, L., Bastos, A., Bastrikov, V., Becker, M., Bopp, L., Buitenhuis, E., Chandra, N., Chevallier, F., Chini, L. P., Currie, K. I., Feely, R. A., Gehlen, M., Gilfillan, D., Gkritzalis, T., Goll, D. S., Gruber, N., Gutekunst, S., Harris, I., Haverd, V., Houghton, R. A., Hurtt, G., Ilyina, T., Jain, A. K., Joetzjer, E., Kaplan, J. O., Kato, E., Klein Goldewijk, K., Korsbakken, J. I., Landschützer, P., Lauvset, S. K., Lefèvre, N., Lenton, A., Lienert, S., Lombardozzi, D., Marland, G., McGuire, P. C., Melton, J. R., Metzl, N., Munro, D. R., Nabel, J. E. M. S., Nakaoka, S.-I., Neill, C., Omar, A. M., Ono, T., Peregon, A., Pierrot, D., Poulter, B., Rehder, G., Resplandy, L., Robertson, E., Rödenbeck, C., Séférian, R., Schwinger, J., Smith, N., Tans, P. P., Tian, H., Tilbrook, B., Tubiello, F. N., van der Werf, G. R., Wiltshire, A. J., and Zaehle, S.: Global Carbon Budget 2019, Earth Syst. Sci. Data, 11, 1783-1838, 2019.

Gan, J., Li, H., Curchitser, E. N., and Haidvogel, D. B.: Modeling South China sea circulation: Response to seasonal forcing regimes, J. Geophys. Res.: Oceans, 111, C06034, 2006.

Gan, J., Li, L., Wang, D., and Guo, X.: Interaction of a river plume with coastal upwelling in the northeastern South China Sea, Cont. Shelf Res., 29, 728-740, 2009.

Gan, J., Lu, Z., Dai, M., Cheung, A. Y. Y., Liu, H., and Harrison, P.: Biological response to intensified upwelling and to a river plume in the northeastern South China Sea: A modeling study, J. Geophys. Res.: Oceans, 115, C09001, 2010.

Guo, X. and Wong, G.: Carbonate chemistry in the Northern South China Sea shelf-sea in June 2010, Deep Sea Res. II, 117, 119-130, 2015.

Han, A. Q., Dai, M. H., Gan, J. P., Kao, S. J., Zhao, X. Z., Jan, S., Li, Q., Lin, H., Chen, C. T. A., and Wang, L.: Inter-shelf nutrient transport from the East China Sea as a major nutrient source supporting winter primary production on the northeast South China Sea shelf, Biogeosciences, 10, 8159-8170, 2013.

Hu, J., Kawamura, H., Li, C., Hong, H., and Jiang, Y.: Review on current and seawater volume transport through the Taiwan Strait, J. Oceanogr., 66, 591-610, 2010.

Jones, S. D., Quéré, C., and Rödenbeck, C.: Spatial decorrelation lengths of surface ocean fCO_2 results in NetCDF format, Global Biogeochem. Cy., 26, GB2042, 2014.

Jo, Y., Dai, M., Zhai, W., Yan, X., and Shang, S.: On the Variations of Sea Surface pCO2 in the Northern South China Sea - A

https://doi.org/10.5194/essd-2022-322
Preprint. Discussion started: 4 October 2022

520 Remote Sensing Based Neural Network Approach, J. Geophys. Res.: Oceans, 117, C08022, 2012.
521 Landschützer, P., Gruber, N., and Bakker, D.: Decadal variations and trends of the global ocean carbon sink, Global Biogeochem.
522 Cy., 30, 1396-1417, 2016.
523 Landschützer, P., Gruber, N., and Bakker, D. C. E.: An updated observation-based global monthly gridded sea surface pCO_2 and
524 air-sea CO_2 flux product from 1982 through 2015 and its monthly climatology, Dataset, 2017.
525 Laruelle, G., Lauerwald, R., Pfeil, B., and Regnier, P.: Regionalized global budget of the CO_2 exchange at the air-water interface
526 in continental shelf seas, Global Biogeochem. Cy., 28, 1199-1214, 2015.
527 Landschützer, P., Bakker, D. C. E., Gruber, N., and Schuster, U.: Recent variability of the global ocean carbon sink, Global
528 Biogeochem. Cy., 28, 927-949, 2014.
529 Lefèvre, N., Watson, A., and Waston, A.,: A comparison of multiple regression and neural network techniques for mapping in situ
530 pCO_2 data, Tellus B, 57, 375-384, 2005.
531 Lefévre, N., Watson, A. J., and Watson, A. R.: A comparison of multiple regression and neural network techniques for mapping in
532 situ pCO_2 data, Tellus B: Chemical and Physical Meteorology, Dataset, 2017.
533 Li, Y., Xie, P., Tang, Z., Jiang, T., and Qi, P.: SVM-Based Sea-Surface Small Target Detection: A False-Alarm-Rate-Controllable
534 Approach, IEEE Geosc.i Remote S., 16, 1225-1229, 2019.
535 Li, H., Wiesner, M. G., Chen, J., Lin, Z., Zhang, J., and Ran, L.: Long-term variation of mesopelagic biogenic flux in the central
536 South China Sea: Impact of monsoonal seasonality and mesoscale eddy, Deep Sea Res. I, 126, 62-72, 2017.
537 Li, Q., Guo, X., Zhai, W., Xu, Y., Dai, M.: Partial pressure of CO_2 and air-sea CO_2 fluxes in the South China Sea: Synthesis of an
538 18-year dataset, Prog. Oceanogr., 182, 102272, 2020.
539 Luo, X., Hao, W., Zhe, L., and Liang, Z.: Seasonal variability of air-sea CO_2 fluxes in the Yellow and East China Seas: A case
540 study of continental shelf sea carbon cycle model, Cont. Shelf Res., 107, 69-78, 2015.
541 Mongwe, N. P., Chang, N., and Monteiro, P.: The seasonal cycle as a mode to diagnose biases in modelled CO_2 fluxes in the
542 Southern Ocean, Ocean Model., 106, 90-103, 2016.
543 Park, J. H.: Effects of Kuroshio intrusions on nonlinear internal waves in the South China Sea during winter, J. Geophys. Res.:
544 Oceans, 118, 7081-7094, 2013.
545 Qin, H., Chen, G., Wang, W., Wang, D., and Zeng, L.: Validation and application of MODIS-derived SST in the South China Sea,
546 Int. J. Remote Sens., 35, 4315-4328, 2014.
547 Rödenbeck, C., Bakker, D. C. E., Gruber, N., Iida, Y., Jacobson, A. R., Jones, S., Landschützer, P., Metzl, N., Nakaoka, S., and
548 Olsen, A.: Data-based estimates of the ocean carbon sink variability-first results of the Surface Ocean pCO_2 Mapping
549 intercomparison (SOCOM), Biogeosciences, 12, 14-49, 2015.
550 Sheu, D. D., Chou, W. C., Wei, C. L., Hou, W. P., Wong, G., and Hsu, C. W.: Influence of El Niño the sea-to-air CO_2 flux at the

https://doi.org/10.5194/essd-2022-322
Preprint. Discussion started: 4 October 2022

SEATs time-series site, northern South China Sea, J. Geophys. Res.: Oceans, 115, C10021, 2010.

Tahata, M., Sawaki, Y., Ueno, Y., Nishizawa, M., Yoshida, N., Ebisuzaki, T., Komiya, T., and Maruyama, S.: Three-step modernization of the ocean: Modeling of carbon cycles and the revolution of ecological systems in the Ediacaran/Cambrian periods, Geosci. Front., 6, 121-136, 2015.

Telszewski, M., Chazottes, A., Schuster, U., Watson, A. J., and Wanninkhof, R.: Estimating the monthly pCO_2 distribution in the North Atlantic using a self-organizing neural network, Biogeosciences, 6, 1405-1421, 2009.

Wang, G., Shen, S. S. P., Chen, Y., Bai, Y., Qin, H., Wang, Z., Chen, B., Guo, X., and Dai, M.: Feasibility of reconstructing the basin-scale sea surface partial pressure of carbon dioxide from sparse in situ observations over the South China Sea, Earth Syst. Sci. Data, 13, 1403-1417, 2021.

Wanninkhof, R., Park, G. H., Takahashi, T., Sweeney, C., Feely, R., Nojiri, Y., Gruber, N., Doney, S. C., Mckinley, G. A., and Lenton, A.: Global ocean carbon uptake: magnitude, variability and trend, Biogeosciences, 10, 1983-2000, 2013

Wang, Z., Wang, G., Guo, X., Bai, Y., Xu, Y., and Dai, M.: Spatial reconstruction of long-term (2003-2020) sea surface pCO_2 in the South China Sea using a machine learning based regression method aided by empirical orthogonal function analysis, Github, https://github.com/Elricriven/co2data.

Xu, X., Zang, K., Zhao, H., Zheng, N., Huo, C., and Wang, J.: Monthly CO_2 at A4HDYD station in a productive shallow marginal sea (Yellow Sea) with a seasonal thermocline: Controlling processes, J. Marine Syst., 159, 89-99, 2016.

Jo, Y., Dai, M., Zhai, W., Yan, X., and Shang, S.: On the variations of sea surface pCO_2 in the northern South China Sea: A remote sensing based neural network approach, J. Geophys. Res.: Oceans, 117, C08022, 2012.

Yang, W., Guo, X., Cao, Z., Wang, L., Guo, L., Huang, T., Li, Y., Xu, Y., Gan, J., and Dai, M.: Seasonal dynamics of the carbonate system under complex circulation schemes on a large continental shelf: The northern South China Sea, Prog Oceanogr., 197, 1026-1045, 2021.

Yu, Z., Shang, S., Zhai, W., and Dai, M.: Satellite-derived surface water pCO_2 and air-sea CO_2 fluxes in the northern South China Sea in summer, Prog. Nat. Sci., 19, 775-779, 2009.

Zeng, J., Matsunaga, T., Saigusa, N., Shirai, T., Nakaoka, S. I., and Tan, Z. H.: Technical note: Evaluation of three machine learning models for surface ocean CO_2 mapping, Ocean Sci., 13, 303-313, 2017.

Zhai, W., Dai, M., Cai, W. J., Wang, Y., and Hong, H.: The partial pressure of carbon dioxide and air-sea fluxes in the northern South China Sea in spring, summer and fall, Mar. Chem., 96, 87-97, 2005.

Zhai, W. D., Dai, M. H., Chen, B. S., Guo, X. H., Li, Q., Shang, S. L., Zhang, C. Y., Cai, W. J., and Wang, D. X.: Seasonal variations of sea-air CO_2 fluxes in the largest tropical marginal sea (South China Sea) based on multiple-year underway measurements, Biogeosciences, 10, 7775-7791, 2013.

Zhang, C., Hu, C., Shang, S., Müller-Karger, F., Yan, L., Dai, M., Huang, B., Ning, X., and Hong, H.: Bridging between SeaWiFS

https://doi.org/10.5194/essd-2022-322
Preprint. Discussion started: 4 October 2022

582 and MODIS for continuity of chlorophyll-a concentration assessments off Southeastern China, Remote Sens. Environ., 102,
583 250-263, 2006.
584 Zhan, Y., Zhang, H., Li, J., and Li, G.: Prediction Method for Ocean Wave Height Based on Stacking Ensemble Learning Model. J.
585 Mar. Sci. Eng., 10, 1150, 2022.
586 Zhu, Y., Shang, S., Zhai, W., and Dai, M.: Satellite-derived surface water pCO_2 and air-sea CO_2 fluxes in the northern South China
587 Sea in summer, Prog. Nat. Sci., 19, 775-779, 2009.